

See discussions, stats, and author profiles for this publication at: <https://www.researchgate.net/publication/258947598>

# Efficient Dual-Modal NIR-to-NIR Emission of Rare Earth Ions Co-doped Nanocrystals for Biological Fluorescence Imaging

ARTICLE in JOURNAL OF PHYSICAL CHEMISTRY LETTERS · FEBRUARY 2013

Impact Factor: 7.46 · DOI: 10.1021/jz302122a

CITATIONS

21

READS

56

10 AUTHORS, INCLUDING:



Jiajia Zhou

China Jiliang University

62 PUBLICATIONS 727 CITATIONS

SEE PROFILE



Batu Ghosh

National Institute for Materials Science

16 PUBLICATIONS 146 CITATIONS

SEE PROFILE



Minoru Fujii

Kobe University

336 PUBLICATIONS 6,480 CITATIONS

SEE PROFILE



Jianrong Qiu

South China University of Technology

691 PUBLICATIONS 11,280 CITATIONS

SEE PROFILE

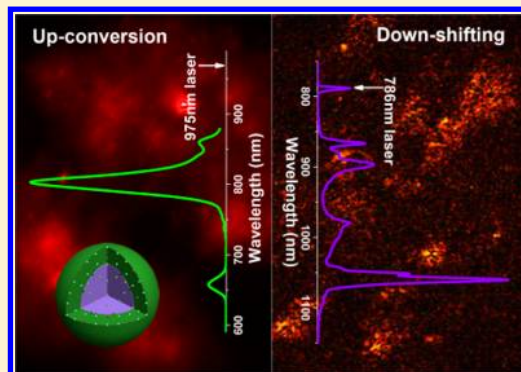
## Efficient Dual-Modal NIR-to-NIR Emission of Rare Earth Ions Co-doped Nanocrystals for Biological Fluorescence Imaging

Jiajia Zhou,<sup>†,‡</sup> Naoto Shirahata,<sup>‡,§</sup> Hong-Tao Sun,<sup>¶</sup> Batu Ghosh,<sup>‡</sup> Makoto Ogawara,<sup>⊥,||</sup> Yu Teng,<sup>†</sup> Shifeng Zhou,<sup>†</sup> Rong Gui Sa Chu,<sup>Δ</sup> Minoru Fujii,<sup>Δ</sup> and Jianrong Qiu<sup>\*,†,‡,#</sup><sup>†</sup>State Key Laboratory of Silicon Materials, Zhejiang University, Hangzhou 310027, China<sup>‡</sup>World Premier International Research Center Initiative for Materials Nanoarchitectonics (MANA), National Institute for Materials Science (NIMS), 1-1 Namiki, Tsukuba, Ibaraki 305-0044, Japan<sup>§</sup>PRESTO, Japan Science and Technology Agency (JST), 4-1-8 Honcho Kawaguchi, Saitama 332-0012, Japan<sup>¶</sup>Division of Materials Science and Engineering, Faculty of Engineering, Hokkaido University, Sapporo 060-8628, Japan<sup>⊥</sup>National Institute for Materials Science (NIMS), 1-2-1 Sengen, Tsukuba-city, Ibaraki 305-0047, Japan<sup>||</sup>Graduate School of Pure and Science and Applied Science, The University of Tsukuba, 1-1-1 Tennodai, Tsukuba, Ibaraki 305-8577, Japan<sup>Δ</sup>Department of Electrical and Electronic Engineering, Kobe University, Kobe 657-8501, Japan<sup>#</sup>State Key Laboratory of Luminescent Materials and Devices, South China University of Technology, Guangzhou 510640, China

## S Supporting Information

**ABSTRACT:** A novel approach has been developed for the realization of efficient near-infrared to near-infrared (NIR-to-NIR) upconversion and down-shifting emission in nanophosphors. The efficient dual-modal NIR-to-NIR emission is realized in a  $\beta$ -NaGdF<sub>4</sub>/Nd<sup>3+</sup>@NaGdF<sub>4</sub>/Tm<sup>3+</sup>–Yb<sup>3+</sup> core–shell nanocrystal by careful control of the identity and concentration of the doped rare earth (RE) ion species and by manipulation of the spatial distributions of these RE ions. The photoluminescence results reveal that the emission efficiency increases at least 2-fold when comparing the materials synthesized in this study with those synthesized through traditional approaches. Hence, these core–shell structured nanocrystals with novel excitation and emission behaviors enable us to obtain tissue fluorescence imaging by detecting the upconverted and down-shifted photoluminescence from Tm<sup>3+</sup> and Nd<sup>3+</sup> ions, respectively. The reported approach thus provides a new route for the realization of high-yield emission from RE ion doped nanocrystals, which could prove to be useful for the design of optical materials containing other optically active centers.

**SECTION:** Spectroscopy, Photochemistry, and Excited States



The development of biocompatible nanoparticles for in vivo imaging is an area that is currently attracting considerable interest across a wide range of science, engineering, and biomedical disciplines.<sup>1–3</sup> In recent years, organic dyes and quantum dots (QDs) have been widely studied for bioimaging applications, and significant advances have been reported.<sup>4–8</sup> For in vivo imaging, developing engineering materials with excitation and emission bands in the near-infrared (NIR) spectral region, especially in the first and second biological windows, is of vital importance due to the lack of efficient endogenous absorbers in this spectral range and the resulting high light penetration depth (on the order of a few millimeters in most tissues).<sup>9–12</sup> However, the number of available NIR emitting dyes is rather limited, and their poor photostability also hinders their application for long-term in vivo bioimaging.<sup>13</sup> Although QDs offer substantial advantages over organic

dyes such as high-efficiency NIR emission, broad absorption spectra coupled to narrow size-tunable emissions, and exceptional resistance to both photobleaching and chemical degradation, the clinical translation has been impeded, owing to concerns regarding the biodegradability of such materials, the toxicity of degradation byproducts, and/or the toxic characteristics of the nanomaterials themselves.<sup>14</sup> Therefore, additional research is needed in order to develop nontoxic or biodegradable nanoparticles with high-yield NIR emission for in vivo bioimaging.

The inherent drawbacks of applying organic dyes and QDs for bioimaging have promoted the development of a new class

**Received:** December 19, 2012

**Accepted:** January 11, 2013

**Published:** January 11, 2013



of probes, that is, rare earth (RE) ions doped nanoparticles. The abundant energy level structures and Laporte-forbidden  $f-f$  electronic transitions of RE ions result in a large Stokes shift, sharp emission bandwidths, long lifetimes (microseconds scale), tunable emissions, and photostability, which render them particularly useful for bioimaging applications.<sup>15–22</sup> In 2008, Prasad et al. proposed the concept of NIR-to-NIR photoluminescence bioimaging.<sup>23</sup> Since then, probes doped with the  $\text{Tm}^{3+}\text{--Yb}^{3+}$  couple have been widely adopted to achieve  $\sim 800$  nm emission by the upconversion (UC) energy transfer (ET) from  $\text{Yb}^{3+}$  upon excitation using the low-cost 980 nm laser diodes.<sup>24–29</sup> Although many studies have demonstrated the successful bioimaging using the RE ions doped probes, most of these prior studies focus on the single-modal NIR-to-NIR emission and ignore the practical spatial distribution of the doped RE ions. However, it is well-known that the nonradiative ET of RE ions on one hand facilitates the effective sensitization of some RE ions by others (e.g., in the case of  $\text{Tm}^{3+}\text{--Yb}^{3+}$  couple) but on the other hand greatly reduces the emission yields (i.e., concentration quenching and nonradiatively cross relaxation of RE ions). As a result, it is important to carefully design the RE ions doping routes in the targeted material systems in order to suppress the energy losses due to the undesirable electronic transitions between RE ions, especially when the performance of RE ions doped materials are approaching their physical limits.

In this Letter, we address the above issues by selectively doping RE ion couples with suitable NIR excitation/emission bands and manipulating their spatial distribution in hexagonal-phase core-shell fluoride nanocrystals. Hereby, we realize simultaneous UC and down-shifting (DS) emissions within the same nanoparticle, which results in an increase of the photoluminescence yield by at least a factor of 2 in comparison with the materials synthesized through the traditionally applied approaches. Finally, we demonstrate NIR-to-NIR biological tissue fluorescence imaging for the first time using the nanoparticles operating in both UC and DS modes.

The hexagonal-phase  $\text{NaGdF}_4$  crystal was chosen as the host system for doping the RE ions due to its outstanding properties in terms of the low phonon energy similar to that of  $\text{NaYF}_4$ , relatively small particle size (less than 20 nm), and uniform morphology.<sup>30</sup> A typical RE ion couple (namely,  $\text{Tm}^{3+}$  and  $\text{Yb}^{3+}$ ) was utilized in order to obtain the desired NIR-to-NIR UC emission because this pair exhibits efficient UC luminescence. In addition,  $\text{Nd}^{3+}$  ions were chosen as the NIR-to-NIR DS emission mode candidates because  $\text{Nd}^{3+}$  exhibits efficient emission at  $\sim 1.06$   $\mu\text{m}$  upon excitation at 740/800 nm.<sup>31</sup> The tridoped sample containing 2 mol %  $\text{Tm}^{3+}$ , 20 mol %  $\text{Yb}^{3+}$ , and 10 mol %  $\text{Nd}^{3+}$  was synthesized by using the coprecipitation method and is hereafter labeled as NTY. The crystal phase was evaluated by using X-ray diffraction (XRD) analysis. The diffraction peaks were in agreement with the standard XRD pattern of hexagonal  $\text{NaGdF}_4$  of JCPDS 27-0699, as shown in Figure 1A. The low-resolution transmission electron microscopy (TEM) image in Figure 1B reveals the uniform and circular cross section of the NTY sample, whereas the high-resolution TEM (HRTEM) image shows the perfect crystallization behavior, in which the (110) lattice plane with 0.30 nm interplanar distances is clearly observed (Figure 1C).

The luminescent properties of the prepared materials were evaluated by dispersing the nanocrystals in cyclohexane with a concentration of 2 mg/mL. NIR emissions are observed under both UC modal excitation at 980 nm and DS modal excitation

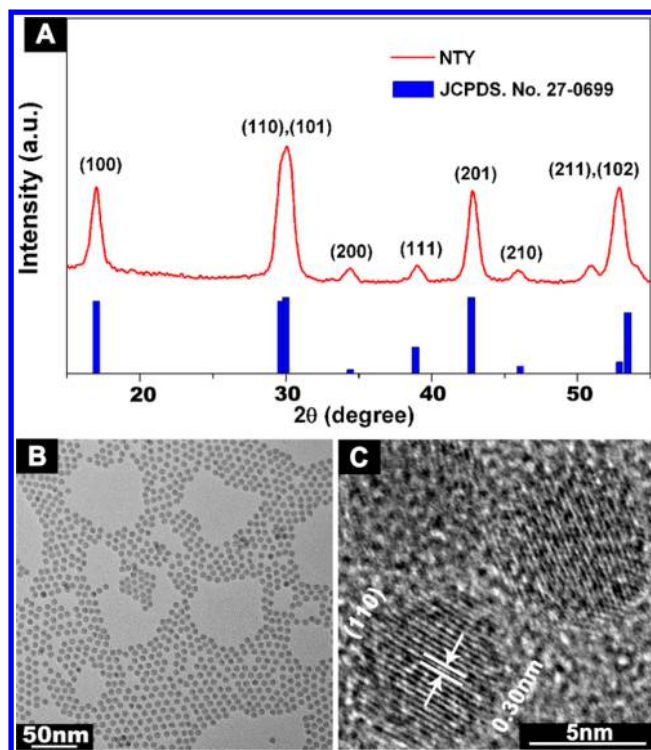


**Figure 1.** (A) XRD pattern of NTY. (B) Low-resolution TEM photo of NTY. (C) HRTEM photo of NTY.

at 740 nm in the tridoped sample NTY. However, the emission intensities are inferior to that of the non-tridoped samples, that is, sample doped with  $\text{Tm}^{3+}$  and  $\text{Yb}^{3+}$  (labeled TY) or samples doped with only  $\text{Nd}^{3+}$  (labeled N). Figure 2A presents the UC emission spectra of TY and NTY samples. The emission bands related to the  $\text{Tm}^{3+}/^1\text{G}_4 \rightarrow ^3\text{F}_4$  and  $^3\text{H}_4 \rightarrow ^3\text{H}_6$  transitions are significantly less intense in the NTY sample compared with those in the TY sample. Similarly, the emission bands of the  $\text{Nd}^{3+}/^4\text{F}_{3/2} \rightarrow ^4\text{I}_{9/2}$  and  $^4\text{F}_{3/2} \rightarrow ^4\text{I}_{11/2}$  transitions in the NTY sample are less intense than those in the N sample (Figure 2B). Interestingly, compared with the N sample, NTY exhibits an additional peak at around 990 nm upon 740 nm excitation. This peak can be ascribed to the  $\text{Yb}^{3+}/^2\text{F}_{5/2} \rightarrow ^2\text{F}_{7/2}$  transition as a result of the ET from  $\text{Nd}^{3+}$  to  $\text{Yb}^{3+}$  through ET1, as illustrated in Figure 2C. The existence of this process is further supported by the combined results of the excitation and time-resolved emission spectra shown in Figures S1 and S2 (Supporting Information).

Förster resonance energy transfer (FRET) refers to the nonradiative transfer of an electronic excitation from a donor to a proximal ground-state acceptor. The transfer takes place when the oscillations of the optically induced electronic coherence on the donor are in resonance with the electronic energy gap of the acceptor, that is, the process generally requires sufficient spectral overlap between donor emission and acceptor absorption bands. In order to describe the luminescence quenching mechanism in the NTY sample, we depicted the energy level diagrams of the  $\text{Nd}^{3+}$ ,  $\text{Tm}^{3+}$ , and  $\text{Yb}^{3+}$  ions in Figure 2C. Owing to the abundant energy levels of  $\text{Nd}^{3+}$  and  $\text{Tm}^{3+}$ , multiple ET processes between every two ions are possible, especially when their spatial distances and energy differences are proper. Detailed comparisons of the UC luminescent spectra of NTY and TY samples are shown in Figure S3 (Supporting Information). It is observed that all of



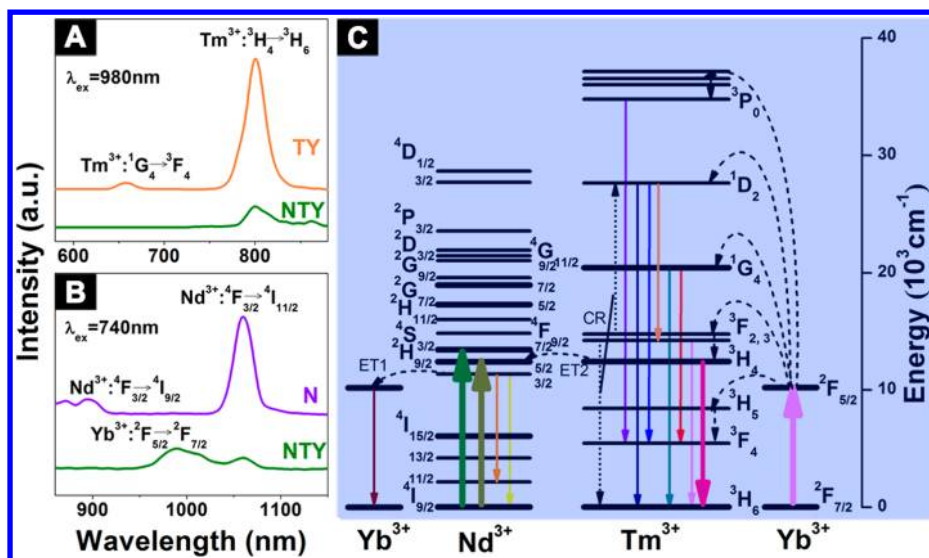


**Figure 2.** (A) UC emission spectra of NTY and TY under 980 nm excitation. (B) DS emission spectra of NTY and N under 740 nm excitation. (C) Energy level diagrams of  $\text{Nd}^{3+}$ ,  $\text{Tm}^{3+}$ , and  $\text{Yb}^{3+}$  ions.

the  $\text{Tm}^{3+}$  UC luminescence is quenched in the NTY sample. This implies that the quenching of  $\text{Tm}^{3+}$  luminescence is closely correlated with the presence of  $\text{Nd}^{3+}$  ions because the highly excited energy levels of  $\text{Tm}^{3+}$  are further excited by a ladder-like energy population from  $\text{Yb}^{3+}$ . On the basis of the energy matching conditions, possible ET route ET2 ( $\text{Tm}^{3+}/{}^3\text{H}_4 + \text{Nd}^{3+}/{}^4\text{I}_{9/2} \rightarrow \text{Tm}^{3+}/{}^3\text{H}_6 + \text{Nd}^{3+}/{}^4\text{F}_{5/2}, {}^2\text{H}_{9/2}$ ) exists in the NTY sample, as illustrated in Figure 2C. The occurrence of ET2 is a result of the high population density in donor-level  ${}^3\text{H}_4$  and the strong absorption transition  ${}^4\text{I}_{9/2} \rightarrow {}^4\text{F}_{5/2}, {}^2\text{H}_{9/2}$  of the acceptor.<sup>32</sup> This has previously been reported in refs 33 and 34. In the case of the DS mode, the quenching of  $\text{Nd}^{3+}$  emission is not solely due to the ET from  $\text{Nd}^{3+}$  to  $\text{Yb}^{3+}$ , but it is also a result of the inverse process of ET2, that is, from  $\text{Nd}^{3+}$  to  $\text{Tm}^{3+}$ . The latter is revealed by the photoluminescence results displayed in Figure S4 (Supporting Information).

In order to inhibit the occurrence of unwanted ET, we have tailored the spatial distribution of the doped RE ions in the material.<sup>21,35</sup> Concentration quenching is frequently caused by ET from one activator to another.<sup>36</sup> Hence, in the NTY sample, the short spatial distances between the  $\text{Tm}^{3+}$  and  $\text{Nd}^{3+}$  ions, caused by high local concentrations, result in the quenching of the emissions from both  $\text{Tm}^{3+}$  and  $\text{Nd}^{3+}$ . The critical distance ( $R_c$ ) between  $\text{Tm}^{3+}$  and  $\text{Nd}^{3+}$  ions can be calculated using the relation proposed by Blasse and Grabmaier<sup>37</sup>

$$R_c \approx 2 \left( \frac{3V}{4\pi X_c N} \right)^{1/3} \quad (1)$$

where  $X_c$  denotes the total concentration of dopants,  $N$  the number of available sites for the dopant in the unit cell, and  $V$  the volume of the unit cell. For a  $\beta\text{-NaGdF}_4$  host, which is isostructural with a  $\beta\text{-NaYF}_4$  crystal with space group  $P6_3/m$ , two different sites with nine-fold coordination exist, one occupied only by  $\text{Gd}^{3+}$  and another one occupied by  $\text{Gd}^{3+}$  and  $\text{Na}^+$  in a 1:1 ratio.<sup>38,39</sup> This is seen in the crystal structure shown in Figure 3A.  $N$  is equal to 1.5 for the RE ion dopants used here, which is a commonly used model for the hexagonal phase.<sup>40</sup> Assuming that the lattice parameters remain approximately constant following  $\text{Tm}^{3+}$  and  $\text{Nd}^{3+}$  doping, the value of  $V$ , obtained from the XRD results, is equal to  $130.5 \text{ \AA}^3$ .

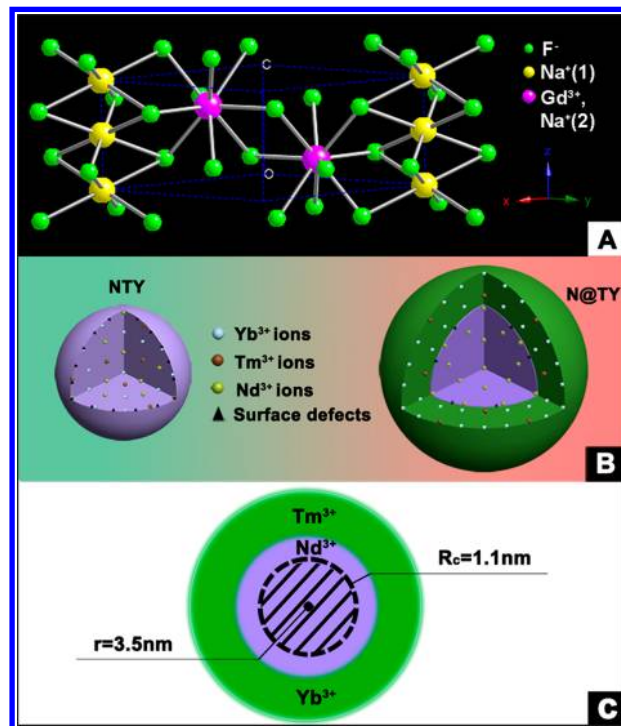


**Figure 3.** (A) Crystal structure of  $\beta\text{-NaGdF}_4$ . (B) Illustration of the spatial structure of NTY and N@TY. (C) Cross section of the core-shell structure with spatial doping.

Because  $X_c$  is equal to 0.12, the critical distance  $R_c$  is calculated to be  $11.1 \text{ \AA}$ . As shown in Figure 1B,C, we have found that the diameter of the spherical nanocrystal is equal to  $\sim 7 \text{ nm}$ . To shield the ET between  $\text{Tm}^{3+}$  and  $\text{Nd}^{3+}$  ions, spatial isolation may thus be a viable option because the nanocrystal diameter is about six times larger than the value of  $R_c$ . Furthermore, given the higher concentration and richer energy levels of  $\text{Nd}^{3+}$  ions compared to those of  $\text{Tm}^{3+}$  ions, the  $\text{Nd}^{3+}$  ions are more likely to be affected by luminescence quenching, especially the  $\text{Nd}^{3+}$  ions existing in the surface sites of the nanoparticle. Previous results in the literature have revealed that the epitaxial growth of a shell layer, with the same composition ( $\text{NaGdF}_4$ ) as the

core, can convert surface sites completely into interior sites.<sup>41</sup> As a consequence, the enhancement of the emission intensity can be obtained through the surface passivation effect. Therefore, in Figure 3B, we show the designed spatial structure of the nanocrystals with the Nd<sup>3+</sup> ions residing in the core and the Tm<sup>3+</sup>–Yb<sup>3+</sup> couple residing in the shell layer. This structuring also partially passivates previous surface defects as a result of the shell protection. In Figure 3C, the cross section of the core–shell structured nanoparticle is shown, including a comparison of the radius of the particle  $r$  with the critical ET distance  $R_c$ .

On the basis of the above analysis, the core–shell structured sample (labeled N@TY) with 10 mol % Nd<sup>3+</sup> in the core and 2 mol % Tm<sup>3+</sup>–20 mol % Yb<sup>3+</sup> in the shell was synthesized in order to optimize the NIR-to-NIR emission yield. Comparative TEM photos of NTY and N@TY samples are shown in Figure 4A,B. The homogeneous epitaxial growth results in a difference

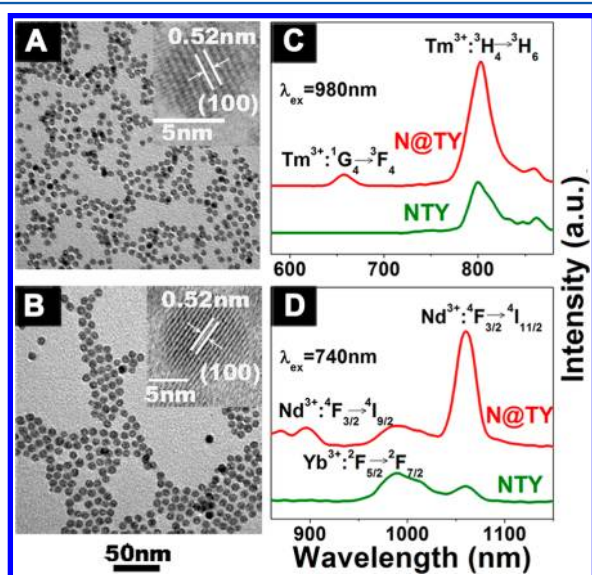


**Figure 4.** (A) TEM photo of NTY (inset: HRTEM photo of NTY). (B) TEM photo of N@TY (inset: HRTEM photo of N@TY). (C) UC emission spectra of N@TY and NTY under 980 nm excitation. (D) DS emission spectra of N@TY and NTY under 740 nm excitation.

in the particle size, whereas no detectable lattice distortion is observed. The UC and DS emission spectra of N@TY and NTY samples are shown in Figure 4C and D, respectively. The emission efficiency increases by at least a factor of 2 and 7 for Tm<sup>3+</sup>/<sup>3</sup>H<sub>4</sub> → <sup>3</sup>H<sub>6</sub> and Nd<sup>3+</sup>/<sup>4</sup>F<sub>3/2</sub> → <sup>4</sup>I<sub>9/2</sub> transitions, respectively, when comparing the homogeneous nanoparticles (NTY) with the core–shell structured nanoparticles (N@TY). The smaller efficiency enhancement of the Tm<sup>3+</sup> related transition relative to that of Nd<sup>3+</sup> in N@TY could be ascribed to two factors. First, Tm<sup>3+</sup> ions doped in the shell layer do not exhibit any surface passivation. Second, cross relaxation (CR in Figure 2C) can occur between Tm<sup>3+</sup> internal levels, which quench the Tm<sup>3+</sup>/<sup>3</sup>H<sub>4</sub> → <sup>3</sup>H<sub>6</sub> transition (Figure S3, Supporting Information). However, most importantly, the deleterious ET from Tm<sup>3+</sup> to Nd<sup>3+</sup> has been almost completely shielded in the core–shell structured sample under UC modal excitation at 980 nm, which is further supported by the spectral data in Figure S3 (Supporting Information). This is not only a result of the spatially separated doping of the Tm<sup>3+</sup> and Nd<sup>3+</sup> ions but also a

result of the increase in spatial size of the 2 mol % Tm<sup>3+</sup> ions distribution, that is, ~517 nm<sup>3</sup> in N@TY (~2 nm in shell thickness) versus ~180 nm<sup>3</sup> in NTY (~7 nm in diameter). However, the ET from Nd<sup>3+</sup> to Yb<sup>3+</sup> partially remains in the N@TY sample under DS modal excitation at 740 nm. This is ascribed to the rapid energy migration resonantly across the Nd<sup>3+</sup> ions to the core–shell interface, where it is then transferred to Yb<sup>3+</sup> in the shell given the high concentrations of 10 mol % Nd<sup>3+</sup> and 20 mol % Yb<sup>3+</sup>.

Complete optical characterization includes measurements of the fluorescence lifetime, and more importantly, the fluorescence lifetime is another important factor for identifying potential probes for biolabeling, in which the longer fluorescence lifetime indicates improved suitability of a RE-doped probe, especially for the DS emission mode. Figure 5

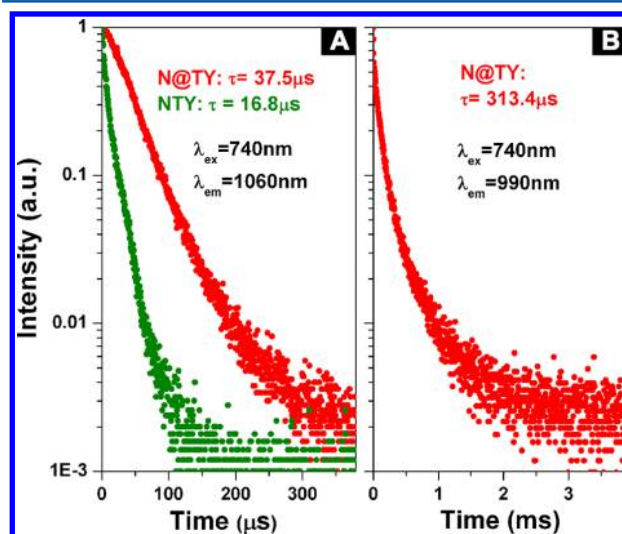


**Figure 5.** (A) Decay curves of Nd<sup>3+</sup> emission at 1060 nm by excitation at 740 nm in N@TY and NTY samples. (B) Decay curve of Yb<sup>3+</sup> emission at 990 nm by excitation at 740 nm in N@TY.

shows the decay curves for DS luminescence in both N@TY and NTY samples. As shown in Figure 5A, the lifetime of the Nd<sup>3+</sup> NIR emission at 1060 nm upon 740 nm excitation is significantly longer in the N@TY sample than that in the NTY sample. The decay curves can be fitted with multiexponential decay

$$I(t) = A_1 \exp\left(-\frac{t}{t_1}\right) + A_2 \exp\left(-\frac{t}{t_2}\right) + A_3 \exp\left(-\frac{t}{t_3}\right) \quad (2)$$

where  $I$  is the luminescence intensity,  $t_i$  is the lifetime, and  $A_i$  is a constant. For comparison, the average lifetimes ( $\langle\tau\rangle$ ) are calculated using the relationship  $\langle\tau\rangle = \sum_i A_i \tau_i^2 / \sum_i A_i \tau_i$ .<sup>42</sup> This gives values of 37.5 and 16.8  $\mu$ s for N@TY and NTY samples, respectively, suggesting that the emission yield is enhanced following adoption of the core–shell structure and adjusting the spatial distribution of the RE ions. This result is consistent with the steady-state DS spectra shown in Figure 4D. Figure 5B shows the decay curve of the Yb<sup>3+</sup> NIR emission at 990 nm upon 740 nm excitation in the N@TY sample. The lifetime of this emission is ~313  $\mu$ s, which is about 18 times longer than the lifetime of Nd<sup>3+</sup> in the NTY sample under excitation at 740 nm (16.8  $\mu$ s). In other words, in the core–shell structured sample, the ET from Nd<sup>3+</sup> to Yb<sup>3+</sup> under the DS emission

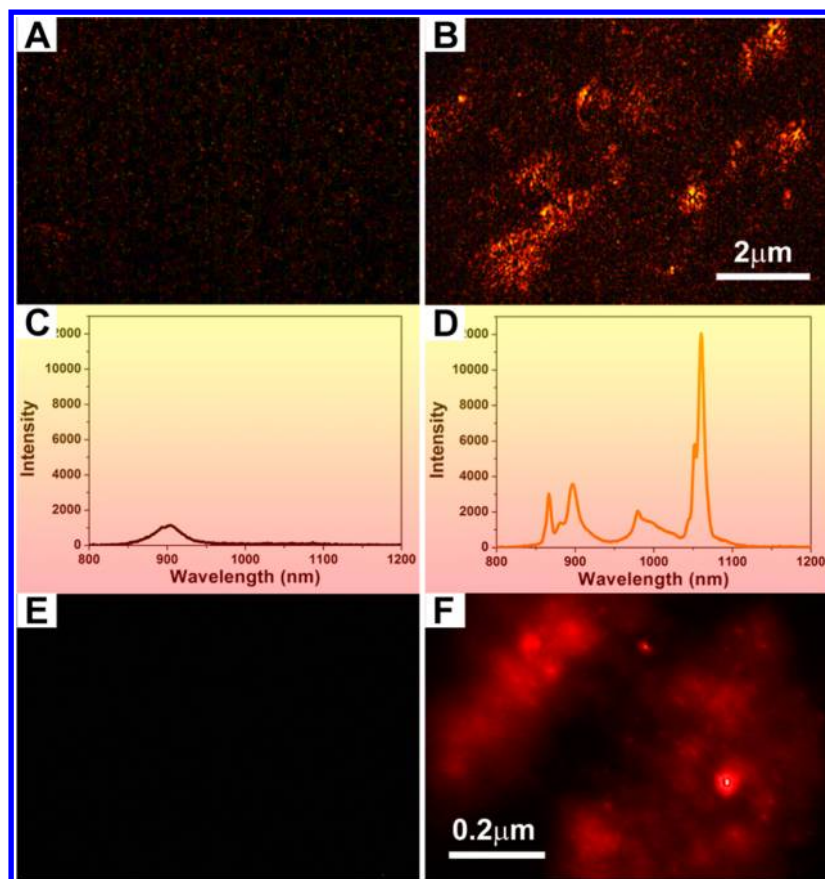


**Figure 6.** Biological tissue fluorescence images and spectra: (A,C) before and (B,D) after injection of N@TY under DS emission mode; (E) before and (F) after injection of N@TY under UC emission mode.

mode exhibits a NIR fluorescence lifetime that is much longer than that of most semiconductor QDs and traditional organic dyes.<sup>43–45</sup> The long-lived emission behavior of the core-shell structured sample suggests that such nanoparticles have potential for lifetime bioimaging.

To examine whether the emission from the synthesized nanoparticles is sufficiently strong for practical bioimaging applications, we have obtained dual-modal imaging by using chicken breast tissue injected with N@TY nanocrystals.<sup>46</sup> The results are shown in Figure 6A–D for the DS mode and in Figure 6E,F for the UC mode. Upon injection of the N@TY nanocrystals, the signal from the tissue increases substantially compared with that prior to injection (compare Figure 6A and B). It should be noted that the images and spectra were acquired under the excitation of a 786 nm laser diode (Figure 6A–D), although 786 nm is not the most proper excitation wavelength and the CCD camera has low sensitivity in the spectral range from 1000 to 1100 nm. The broad emission peak at around 900 nm from the tissue without N@TY nanocrystals results from the autofluorescence of the tissue (Figure 6C). However, it has no pronounced influence on the imaging due to its weak intensity in comparison with the signal from the nanocrystals (Figure 6C,D). The differences in the emission peaks before and after N@TY nanocrystal injection are ascribed to the corresponding transitions of Nd<sup>3+</sup> and Yb<sup>3+</sup> ions in the N@TY sample, which is consistent with the emission spectrum directly measured in N@TY solution (Figure 4D). It should be noted that the tissue autofluorescence is inevitable in the DS imaging mode, though the endogenous absorbers possess weak absorbance of the NIR light. Fortunately, we can obtain a clear

image using core-shell nanoparticles owing to their greatly improved emission yield. For the UC mode, we observe excellent signal-to-noise ratio due to the fact that the tissue autofluorescence is suppressed effectively in the anti-Stokes mode. Finally, it should be noted that the images obtained through DS modes (Figure 6B) and UC modes (Figure 6F) are not comparable because they were acquired using two different imaging systems with different sensitivities (for details, see the Supporting Information).

According to the absorbance analysis of the endogenous absorbers in tissues, water has much lower absorbance near 740/800 nm relative to that at ~980 nm, while hemoglobin exhibits the opposite tendency in the NIR region.<sup>47</sup> Excitation at 740/800 nm is thus better for imaging of skin tissue because water has a strong absorption at around ~980 nm. In this regard, the optimized core-shell structured nanocrystal is most powerful in its DS imaging mode by the incorporation of Nd<sup>3+</sup> dopants, considering its strong absorption at around 740/800 nm and its intense down-shifted emission at 1060 nm. However, when hemoglobin dominates in the tissue (e.g., in blood tissue), the DS imaging mode is apparently disadvantageous due to the tissue autofluorescence, although DS emission efficiency is always much higher than that of UC. Luckily, in order to circumvent this, we could trigger the UC imaging mode of the dual-modal nanoparticles under the excitation of a low-cost commercially available 980 nm laser diode. Hence, the notable values of the core-shell structured nanoparticles prepared by controlling the spatial distributions of the doped RE ions lie not only in their enhanced emission yields but also



in the relaxation of the requirements of the excitation sources for both UC and DS dual-modal imaging.

In conclusion, we have reported an efficient dual-modal NIR-to-NIR emission by controlling the type and spatial distribution of RE ion species in NaGdF<sub>4</sub>-based nanocrystals. The valuable UC luminescence by ET from Yb<sup>3+</sup> to Tm<sup>3+</sup> and DS emission from Nd<sup>3+</sup> were simultaneously obtained in a single nanocrystal. Furthermore, we have optimized the photophysical properties by careful control of the spatial distribution of the RE ions by preparing core-shell structured nanocrystals. This leads to a remarkable enhancement of the fluorescence emission intensity and a longer fluorescence lifetime. By using the core-shell structured sample, we have demonstrated the applicability of the synthesized materials for biological tissue fluorescence imaging in both DS and UC emission modes. The dual-modal NIR-to-NIR emission is thus providing a platform for promising applications within the field of biolabeling.

## EXPERIMENTAL SECTION

**Reagents.** GdCl<sub>3</sub>·6H<sub>2</sub>O (99.99%), NdCl<sub>3</sub>·6H<sub>2</sub>O (99.99%), TmCl<sub>3</sub>·6H<sub>2</sub>O (99.99%), YbCl<sub>3</sub>·6H<sub>2</sub>O (99.99%), NaOH, 1-octadecene (90%), and oleic acid (90%) were purchased from Sigma-Aldrich. NH<sub>4</sub>F and cyclohexane were purchased from Wako Pure Chemical Industries, Ltd. All of the chemicals were used as starting materials without further purification.

**Synthesis of  $\beta$ -NaGdF<sub>4</sub>.** Nd<sup>3+</sup> (N) (10 mol %),  $\beta$ -NaGdF<sub>4</sub>/2 mol % Tm<sup>3+</sup>–20 mol % Yb<sup>3+</sup> (TY),  $\beta$ -NaGdF<sub>4</sub>/10 mol % Nd<sup>3+</sup>–2 mol % Tm<sup>3+</sup>–20 mol % Yb<sup>3+</sup> (NTY), and  $\beta$ -NaGdF<sub>4</sub>/10 mol % Nd<sup>3+</sup>@ NaGdF<sub>4</sub>/2 mol % Tm<sup>3+</sup>–20 mol % Yb<sup>3+</sup> (N@TY) nanocrystals were adapted from the previous report for  $\beta$ -NaGdF<sub>4</sub>/Tm<sup>3+</sup>–Yb<sup>3+</sup>@ NaGdF<sub>4</sub>/Eu<sup>3+</sup> nanocrystals.<sup>48</sup>

**Synthesis of  $\beta$ -NaGdF<sub>4</sub>/Nd<sup>3+</sup> Nanocrystals.** In a typical experiment, 0.45 mmol GdCl<sub>3</sub>·6H<sub>2</sub>O and 0.05 mmol NdCl<sub>3</sub>·6H<sub>2</sub>O were mixed with 4 mL of oleic acid (OA) and 16 mL of 1-octadecene in a 100 mL three-neck round-bottom flask. The resulting mixture was heated to 155 °C under Ar flow with constant stirring for 90 min to form a clear solution and then cooled down to room temperature. Thereafter, 10 mL of methanol solution containing 1.8 mmol NH<sub>4</sub>F and 1.8 mmol NaOH was added, and the solution was stirred at 50 °C for 30 min. After methanol was evaporated, the solution was heated to 300 °C under Ar flow with vigorous stirring for 60 min and then cooled down to room temperature. The obtained nanocrystals were precipitated by addition of 15 mL of acetone, collected by centrifugation, washed with ethanol several times, and finally redispersed in cyclohexane.

**Synthesis of  $\beta$ -NaGdF<sub>4</sub>/Nd<sup>3+</sup>@NaGdF<sub>4</sub>/Tm<sup>3+</sup>–Yb<sup>3+</sup> Core-Shell Nanocrystals.** GdCl<sub>3</sub>·6H<sub>2</sub>O (0.39 mmol), TmCl<sub>3</sub>·6H<sub>2</sub>O (0.01 mmol), and YbCl<sub>3</sub>·6H<sub>2</sub>O (0.1 mmol) were added to a 100 mL three-neck round-bottom flask containing 4 mL of OA and 16 mL of 1-octadecene and heated to 155 °C under Ar flow with constant stirring for 90 min to form a clear solution and then cooled down to 80 °C. Thereafter, 0.5 mmol  $\beta$ -NaGdF<sub>4</sub>/Nd<sup>3+</sup> nanocrystals in 6 mL of cyclohexane was added to the above solution. After the removal of cyclohexane, 10 mL of methanol solution containing 1.8 mmol NH<sub>4</sub>F and 1.8 mmol NaOH was added and stirred at 50 °C for 30 min. After methanol was evaporated, the solution was heated to 300 °C under Ar flow with vigorous stirring for 60 min and then cooled down to room temperature. The obtained core-shell nanocrystals were precipitated by addition of 15 mL of acetone,

collected by centrifugation, washed with ethanol several times, and finally redispersed in cyclohexane.

## ASSOCIATED CONTENT

### Supporting Information

Instrumentations parameters for XRD, TEM, HRTEM, steady- and transient-state photoluminescence, and biological tissue fluorescent imaging measurements. Excitation spectra of N@TY monitored at 1060 and 990 nm. Time-resolved emission spectra of N@TY under 740 nm excitation. Visible-to-NIR emission spectra of UC luminescence of N@TY, NTY, and TY under excitation at 980 nm. This material is available free of charge via the Internet at <http://pubs.acs.org>.

## AUTHOR INFORMATION

### Corresponding Author

\*E-mail: [qjr@zju.edu.cn](mailto:qjr@zju.edu.cn).

### Notes

The authors declare no competing financial interest.

## ACKNOWLEDGMENTS

This work was financially supported by the National Natural Science Foundation of China (Grants 51132004, 51072054, and 51102209) and the National Basic Research Program of China (2011CB808100). We appreciate Professor Morten Mattrup Smedskj of Aalborg University, Denmark for his kind suggestions on the manuscript.

## REFERENCES

- (1) Michalet, X.; Pinaud, F. F.; Bentolila, L. A.; Tsay, J. M.; Doose, S.; Li, J. J.; Sundaresan, G.; Wu, A. M.; Gambhir, S. S.; Weiss, S. Quantum Dots for Live Cells, In Vivo Imaging, and Diagnostics. *Science* **2005**, *307*, 538–544.
- (2) Resch-Genger, U.; Grabolle, M.; Cavaliere-Jaricot, S.; Nitschke, R.; Nann, T. Quantum Dots versus Organic Dyes as Fluorescent Labels. *Nat. Methods* **2008**, *5*, 763–775.
- (3) Frangioni, J. V. In Vivo Near-Infrared Fluorescence Imaging. *Curr. Opin. Chem. Biol.* **2003**, *7*, 626–634.
- (4) Kumar, R.; Roy, I.; Ohulchanskyy, T. Y.; Vathy, L. A.; Bergey, E. J.; Sajjad, M.; Prasad, P. N. In Vivo Biodistribution and Clearance Studies Using Multimodal Organically Modified Silica Nanoparticles. *ACS Nano* **2010**, *4*, 699–708.
- (5) Lim, Y. T.; Kim, S.; Nakayama, A.; Stott, N. E.; Bawendi, M. G.; Frangioni, J. V. Selection of Quantum Dot Wavelengths for Biomedical Assays and Imaging. *Mol. Imaging* **2003**, *2*, 50–64.
- (6) Gao, X. H.; Cui, Y. Y.; Levenson, R. M.; Chung, L. M.; Nie, S. M. In Vivo Cancer Targeting and Imaging with Semiconductor Quantum Dots. *Nat. Biotechnol.* **2004**, *22*, 969–976.
- (7) Yong, K. T.; Roy, I.; Ding, H.; Bergey, E. J.; Prasad, P. N. Biocompatible Near-Infrared Quantum Dots as Ultrasensitive Probes for Long-Term In Vivo Imaging Applications. *Small* **2009**, *5*, 1997–2004.
- (8) He, Y.; Zhong, Y. L.; Su, Y. Y.; Lu, Y. M.; Jiang, Z. Y.; Peng, F.; Xu, T. T.; Su, S.; Huang, Q.; Fan, C. H.; et al. Water-Dispersed Near-Infrared-Emitting Quantum Dots of Ultrasmall Sizes for In Vitro and In Vivo Imaging. *Angew. Chem., Int. Ed.* **2011**, *50*, 5695–5698.
- (9) KÖNIG, K. Multiphoton Microscopy in Life Sciences. *J. Microsc.* **2000**, *200*, 83–104.
- (10) Weissleder, R. A Clearer Vision for In Vivo Imaging. *Nat. Biotechnol.* **2001**, *19*, 316–317.
- (11) Smith, A. M.; Mancini, M. C.; Nie, S. Second Window for In Vivo Imaging. *Nat. Nanotechnol.* **2009**, *4*, 710–711.
- (12) Sun, H.-T.; Yang, J. J.; Fujii, M.; Sakka, Y.; Zhu, Y. F.; Asahara, T.; Shirahata, N.; Ii, M.; Bai, Z. H.; Li, J. G.; et al. Highly Fluorescent Silica-Coated Bismuth-Doped Aluminosilicate Nanoparticles for Near-Infrared Bioimaging. *Small* **2011**, *7*, 199–203.

- (13) Eggeling, C.; Widengren, J.; Rigler, R.; Seidel, C. A. M. Photobleaching of Fluorescent Dyes under Conditions Used for Single-Molecule Detection: Evidence of Two-Step Photolysis. *Anal. Chem.* **1998**, *70*, 2651–2659.
- (14) Park, J. H.; Gu, L.; von Maltzahn, G.; Ruoslahti, E.; Bhatia, S. N.; Sailor, M. J. Biodegradable Luminescent Porous Silicon Nanoparticles for In Vivo Applications. *Nat. Mater.* **2009**, *8*, 331–336.
- (15) Yen, W. M.; Weber, M. J. *Inorganic Phosphors: Compositions, Preparation and Optical Properties*; CRC Press: Boca Raton, FL, 2004.
- (16) Blasse, G.; Grabmaier, B. C. *Luminescent Materials*; Springer: Berlin, Germany, 1994.
- (17) Wang, F.; Liu, X. G. Upconversion Multicolor Fine-Tuning: Visible to Near-Infrared Emission from Lanthanide-Doped NaYF<sub>4</sub> Nanoparticles. *J. Am. Chem. Soc.* **2008**, *130*, 5642–5643.
- (18) Wang, F.; Banerjee, D.; Liu, Y. S.; Chen, X. Y.; Liu, X. G. Upconversion Nanoparticles in Biological Labeling, Imaging, and Therapy. *Analyst* **2010**, *135*, 1839–1854.
- (19) Chan, E. M.; Han, G.; Goldberg, J. D.; Gargas, D. J.; Ostrowski, A. D.; Schuck, P. J.; Cohen, B. E.; Miliron, D. J. Combinatorial Discovery of Lanthanide-Doped Nanocrystals with Spectrally Pure Upconverted Emission. *Nano Lett.* **2012**, *12*, 3839–3845.
- (20) Ostrowski, A. D.; Chan, E. M.; Gargas, D. J.; Katz, E. M.; Han, G.; Schuck, P. J. Controlled Synthesis and Single-Particle Imaging of Bright, Sub-10 nm Lanthanide-Doped Upconverting Nanocrystals. *ACS Nano* **2012**, *6*, 2686–2692.
- (21) Wang, F.; Deng, R. R.; Wang, J.; Wang, Q. X.; Han, Y.; Zhu, H. M.; Chen, X. Y.; Liu, X. G. Tuning Upconversion through Energy Migration in Core–Shell Nanoparticles. *Nat. Mater.* **2011**, *10*, 968–973.
- (22) Chen, G. Y.; Ohulchanskyy, T. Y.; Kachynski, A.; Agren, H.; Prasad, P. N. Intense Visible and Near-Infrared Upconversion Photoluminescence in Colloidal LiYF<sub>4</sub>:Er<sup>3+</sup> Nanocrystals under Excitation at 1490 nm. *ACS Nano* **2011**, *5*, 4981–4986.
- (23) Nyk, M.; Kumar, R.; Ohulchanskyy, T. Y.; Bergey, E. J.; Prasad, P. N. High Contrast in Vitro and in Vivo Photoluminescence Bioimaging Using Near Infrared to Near Infrared Up-Conversion in Tm<sup>3+</sup> and Yb<sup>3+</sup> Doped Fluoride Nanophosphors. *Nano Lett.* **2008**, *8*, 3834–3838.
- (24) Zhou, J.; Sun, Y.; Du, X. X.; Xiong, L. Q.; Hu, H.; Li, F. Y. Dual-Modality in Vivo Imaging Using Rare-Earth Nanocrystals with Near-Infrared (NIR-to-NIR) Upconversion Luminescence and Magnetic Resonance Properties. *Biomaterials* **2010**, *31*, 3287–3295.
- (25) Cao, T. Y.; Yang, Y.; Gao, Y.; Zhou, J.; Li, Z. Q.; Li, F. Y. High-Quality Water-Soluble and Surface-Functionalized Upconversion Nanocrystals as Luminescent Probes for Bioimaging. *Biomaterials* **2011**, *32*, 2959–2968.
- (26) Zhan, Q. Q.; Qian, J.; Liang, H. J.; Somesfalean, G.; Wang, D.; He, S. L.; Zhang, Z. G.; Andersson-Engels, S. Using 915 nm Laser Excited Tm<sup>3+</sup>/Er<sup>3+</sup>/Ho<sup>3+</sup>-Doped NaYbF<sub>4</sub> Upconversion Nanoparticles for In Vitro and Deeper In Vivo Bioimaging without Overheating Irradiation. *ACS Nano* **2011**, *5*, 3744–3757.
- (27) Dong, N.-N.; Pedroni, M.; Piccinelli, F.; Conti, G.; Sbarbati, A.; Ramirez-Hernández, J. E.; Maestro, L. M.; Iglesias-de la Cruz, M. C.; Sanz-Rodriguez, F.; Juarranz, A.; et al. NIR-to-NIR Two-Photon Excited CaF<sub>2</sub>:Tm<sup>3+</sup>,Yb<sup>3+</sup> Nanoparticles: Multifunctional Nanoprobes for Highly Penetrating Fluorescence Bio-Imaging. *ACS Nano* **2011**, *5*, 8665–8671.
- (28) Xing, H. Y.; Bu, W. B.; Ren, Q. G.; Zheng, X. P.; Li, M.; Zhang, S. J.; Qu, H. Y.; Wang, Z.; Hua, Y. Q.; Zhao, K. L.; et al. A NaYbF<sub>4</sub>:Tm<sup>3+</sup> Nanoprobe for CT and NIR-to-NIR Fluorescent Bimodal Imaging. *Biomaterials* **2012**, *33*, 5384–5393.
- (29) Chen, G. Y.; Shen, J.; Ohulchanskyy, T. Y.; Patel, N. J.; Kutikov, A.; Li, Z. P.; Song, J.; Pandey, R. K.; Agren, H.; Prasad, P. N.; et al.  $\alpha$ -NaYbF<sub>4</sub>:Tm<sup>3+</sup>/CaF<sub>2</sub> Core/Shell Nanoparticles with Efficient Near-Infrared to Near-Infrared Upconversion for High-Contrast Deep Tissue Bioimaging. *ACS Nano* **2012**, *6*, 8280–8287.
- (30) Wang, F.; Wang, J.; Liu, X. G. Direct Evidence of a Surface Quenching Effect on Size-Dependent Luminescence of Upconversion Nanoparticles. *Angew. Chem., Int. Ed.* **2010**, *49*, 7456–7460.
- (31) Chen, G. Y.; Ohulchanskyy, T. Y.; Liu, S.; Law, W.-C.; Wu, F.; Swihart, M. T.; Agren, H.; Prasad, P. N. Core/Shell NaGdF<sub>4</sub>:Nd<sup>3+</sup>/NaGdF<sub>4</sub> Nanocrystals with Efficient Near-Infrared to Near-Infrared Downconversion Photoluminescence for Bioimaging Applications. *ACS Nano* **2012**, *6*, 2969–2977.
- (32) Bednarkiewicz, A.; Wawrzynczyk, D.; Nyk, M.; Strek, W. Synthesis and Spectral Properties of Colloidal Nd<sup>3+</sup> Doped NaYF<sub>4</sub> Nanocrystals. *Opt. Mater.* **2011**, *33*, 1481–1486.
- (33) Chen, D. Q.; Yu, Y. L.; Huang, F.; Lin, H.; Huang, P.; Yang, A. P.; Wang, Z. X.; Wang, Y. S. Lanthanide Dopant-Induced Formation of Uniform Sub-10 nm Active-Core/Active-Shell Nanocrystals with Near-Infrared to Near-Infrared Dual-Modal Luminescence. *J. Mater. Chem.* **2012**, *22*, 2632–2640.
- (34) Bluiett, A. G.; Peele, D.; Norman, K.; Brown, E.; Hömmerich, U.; Trivedi, S. B.; Zavada, J. M. Mid-Infrared Emission Characteristics and Energy Transfer Processes in Doubly Doped Tm,Tb:KPb<sub>2</sub>Br<sub>3</sub> and Tm,Nd:KPb<sub>2</sub>Br<sub>3</sub>. *Opt. Mater.* **2011**, *33*, 985–988.
- (35) DiMaio, J. R.; Sabatier, C.; Kokuzov, B.; Ballato, J. Controlling Energy Transfer Between Multiple Dopants within a Single Nanoparticle. *Proc. Natl. Acad. Sci. U.S.A.* **2008**, *105*, 1809–1813.
- (36) Dexter, D. L.; Schulman, J. H. Theory of Concentration Quenching in Inorganic Phosphors. *J. Chem. Phys.* **1954**, *22*, 1063–1070.
- (37) Blasse, G. Energy Transfer in Oxidic Phosphors. *Philips Res. Rep.* **1969**, *24*, 131.
- (38) Krämer, K. W.; Biner, D.; Frei, G.; Güdel, H. U.; Hehlen, M. P.; Lüthi, S. R. Hexagonal Sodium Yttrium Fluoride Based Green and Blue Emitting Upconversion Phosphors. *Chem. Mater.* **2004**, *16*, 1244–1251.
- (39) Wang, F.; Han, Y.; Lim, C. S.; Lu, Y. H.; Wang, J.; Xu, J.; Chen, H. Y.; Zhang, C.; Hong, M. H.; Liu, X. G. Simultaneous Phase and Size Control of Upconversion Nanocrystals through Lanthanide Doping. *Nature* **2010**, *463*, 1061–1065.
- (40) Burns, J. H. Crystal Structure of Hexagonal Sodium Neodymium Fluoride and Related Compounds. *Inorg. Chem.* **1965**, *4*, 881–886.
- (41) Lehmann, O.; Kömpe, K.; Haase, M. Synthesis of Eu<sup>3+</sup>-Doped Core and Core/Shell Nanoparticles and Direct Spectroscopic Identification of Dopant Sites at the Surface and in the Interior of the Particles. *J. Am. Chem. Soc.* **2004**, *126*, 14935–14942.
- (42) Kamat, P. V.; Patrick, B. Photophysics and Photochemistry of Quantized ZnO Colloids. *J. Phys. Chem.* **1992**, *96*, 6829–6834.
- (43) Weon, B. M.; Je, J. H.; Lee, J. -L. Lifetime Dispersion in a Single Quantum Dot. *Appl. Phys. A: Mater. Sci. Process.* **2007**, *89*, 1029–1031.
- (44) Kigel, A.; Brumer, M.; Maikov, G.; Sashchiuk, A.; Lifshitz, E. The Ground-State Exciton Lifetime of PbSe Nanocrystal Quantum Dots. *Superlattices Microstruct.* **2009**, *46*, 272–276.
- (45) Giraud, G.; Schulze, H.; Bachmann, T. T.; Campbell, C. J.; Mount, A. R.; Ghazal, P.; Khondoker, M. R.; Ross, A. J.; Ember, S. W. J.; Ciani, I.; et al. Fluorescence Lifetime Imaging of Quantum Dot Labeled DNA Microarrays. *Int. J. Mol. Sci.* **2009**, *10*, 1930–1941.
- (46) Hessel, C. M.; Rasch, M. R.; Hueso, J. L.; Goodfellow, B. W.; Akhavan, V. A.; Puvanakrishnan, P.; Tunnel, J. W.; Korgel, B. A. Alkyl Passivation and Amphiphilic Polymer Coating of Silicon Nanocrystals for Diagnostic Imaging. *Small* **2010**, *6*, 2026–2034.
- (47) Hamblin, M. R.; Demidova, T. N. Mechanisms of Low Level Light Therapy. *Proc. SPIE* **2006**, *6140*, 614001–614013.
- (48) Liu, Y. S.; Tu, D. T.; Zhu, H. M.; Li, R. F.; Luo, W. Q.; Chen, X. Y. A Strategy to Achieve Efficient Dual-Mode Luminescence of Eu<sup>3+</sup> in Lanthanides Doped Multifunctional NaGdF<sub>4</sub> Nanocrystals. *Adv. Mater.* **2010**, *22*, 3266–3271.